

VOLUME 111
OCTOBER 25, 2007

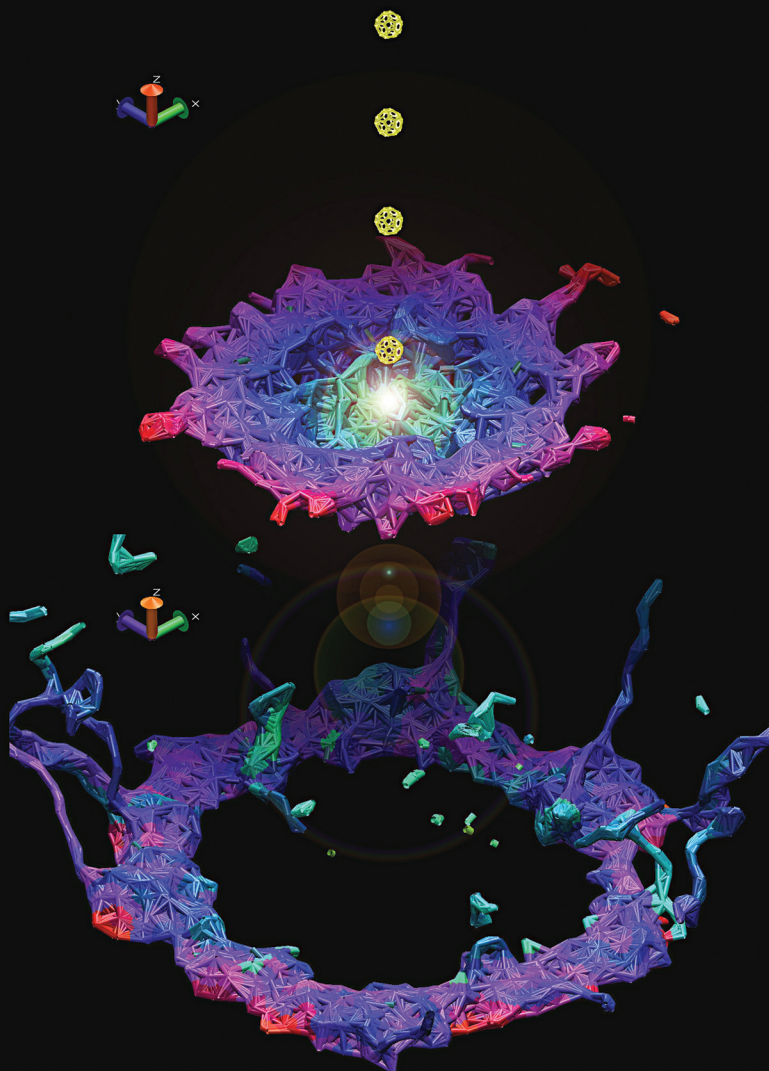
NUMBER 42

<http://pubs.acs.org/JPCC>

THE JOURNAL OF PHYSICAL CHEMISTRY

C

Nanocraters and
Collective Molecular
Emission: Why
Fullerenes Boost
Organic Mass
Spectrometry
(see page XA)



NANOMATERIALS AND INTERFACES

PUBLISHED WEEKLY BY THE AMERICAN CHEMICAL SOCIETY



Sputtering Polymers with Buckminsterfullerene Projectiles: A Coarse-Grain Molecular Dynamics Study[†]

Arnaud Delcorte^{*,‡} and Barbara J. Garrison[§]

PCPM Laboratory, Université Catholique de Louvain, Croix du Sud 1, B-1348 Louvain-la-Neuve, Belgium, and Chemistry Department, The Pennsylvania State University, University Park, Pennsylvania

Received: June 12, 2007; In Final Form: August 9, 2007

Buckminsterfullerene projectiles have demonstrated their outstanding capabilities for the secondary ion mass spectrometric (SIMS) analysis of bulk organic films. In this contribution, we focus on modeling the mechanisms of energy transfer and sputtering induced by kiloelectronvolt C_{60} projectiles in molecular solids and polymers, which are important from the viewpoint of applications and have not been theoretically studied yet. The chosen methodology relies on molecular dynamics (MD) simulations, with a coarse-grained representation of the samples that allows us to dynamically describe over sufficient time intervals the large ensembles of molecules required to properly confine the action induced by 1–10 keV fullerenes in organic targets. For 5 keV bombardment, the simulations explain the transfer of the projectile energy in the topmost layers of the surface, accompanied by the formation of a ~100 Å wide, ~50 Å deep hemispherical crater and the emission of molecules and fragments from the top 30 Å of the surface. Using polyethylene samples with molecular weights ranging from 0.3 kDa up to 14 kDa, the secondary effects of chain length and entanglement on the crater size, sputtering yield, fragmentation, and intact molecule emission are investigated in detail. For instance, it is shown that, in order to be emitted intact, a molecule must be initially confined in the annular region of the forming crater that surrounds the ~30 Å wide energized core where most bond-scissions occur. In contrast, molecules that intersect this track core break upon impact while molecules that extend beyond the size of the crater end up forming the rim or dangling in the vacuum when most of the energy is dissipated. The evolution of the crater size, the sputtered mass and the number of intact molecules with increasing projectile energies (1–10 keV) are reported and connections with experiments are proposed.

1. Introduction

For molecular sample diagnostic, mass spectrometric methods using projectile-induced desorption to form the secondary ion signal constitute a well-established family of techniques with characteristics that are complementary to those of matrix-assisted laser desorption ionization (MALDI) and electrospray ionization (ESI). Even though the accessible mass range of traditional secondary ion mass spectrometry (SIMS), around 10 kDa, is significantly more limited than that of MALDI, the ability to focus liquid metal ion beams (Ga^+ , In^+) down to a spot size of 50 nm in diameter makes ion beams a tool of choice for surface chemical imaging applications. However, with such atomic beams, the characteristic molecular ion signal usually decays quickly with increasing projectile fluence because each primary ion causes damage in the depth of the sample, so that the next ion impinging on a previously probed nanovolume will no longer be able to extract valuable information from that spot. Another problem in organic SIMS is the very low ionization probability of characteristic molecular species. Although a single impact may cause the desorption of a few molecules, only 10^{-7} to 10^{-4} will become naturally ionized and, therefore, detectable. Low ionization probability is common with other techniques such as MALDI, but the small size of the interaction volume and

the performance desired for SIMS imaging makes it a more crucial limitation for organic SIMS. Given the (very low) available signal per unit area, the number of counts that can be obtained per image pixel for molecular ion mappings with submicrometer resolution is usually insufficient.¹

One solution for signal enhancement in particle-induced desorption is to use better “bullets”. In the past decade, reliable polyatomic ion guns (SF_5^+ ,² Au_n^+ ,³ Bi_n^+ ,⁴ C_{60}^+)⁵ have been designed by the manufacturers, and they have been used for fundamental investigations as well as analytical purposes.⁶ Two major advantages of cluster ions are that they induce a strong molecular yield enhancement with respect to isoenergetic atomic ions, particularly for thick organic targets,⁷ and that they allow us to perform depth profiling with retention of the molecular information for a series of sample (reduced damage build-up).⁶ In the growing family of cluster projectiles, SIMS experiments indicate that, on average, C_{60}^+ projectiles provide the largest yield increases for bulk organic samples.⁴

The physics underlying fullerene-induced sputtering has been investigated for various solids, including metal,⁸ silicon,⁹ diamond and graphite,¹⁰ benzene,^{11,12} and water ice targets.¹³ These studies uncovered common effects (mesoscopic motion, crater formation) as well as more sample-specific behaviors (influence of the sample nature, structure, cohesive energy). In general, buckminsterfullerene projectiles transfer all their energy in the topmost layers of the solid, thereby generating a highly excited (superheated) nanovolume and ejecting chunks of material in the gas phase. In contrast with isoenergetic metal clusters of similar mass (Au_{3-4}^+),¹³ fullerenes do not penetrate

* To whom correspondence should be addressed. E-mail: delcorte@pcpm.ucl.ac.be.

[†] Based on a paper presented at the 44th IUVSTA Workshop, Sputtering and Ion Emission by Cluster Ion Beams, Scotland, UK, 23–27 April 2007.

[‡] Université Catholique de Louvain.

[§] The Pennsylvania State University.

TABLE 1: Characteristics of the Icosane and Polyethylene Samples

samples	ICO	PE1	PE3	PE14
formula	C ₂₀ H ₄₂	C ₉₉ H ₂₀₀	C ₂₄₉ H ₅₀₀	C ₁₀₀₀ H ₂₀₀₂
molecular weight (Da)	282	1388	3488	14002
number of molecules	12800	4050	1024	405
total number of CH ₂ /CH ₃ particles	256000	400950	254976	405000
atom-equivalent number cell size	793600	1210950	766976	1215810
- x (Å)	253	264	232	266
- y (Å)	258	301	257	302
- z (Å)	133	153	120	157
density (g/cm ³)	0.90	1.01	1.02	0.98
intermolecular binding energy (eV)				
- total	1.96	8.99	23.46	78.39
- per atom	0.098	0.091	0.094	0.078
number of trajectories at 5 keV	9	5	9	1
other energies	NA	1, 2 and 10 keV	NA	NA

beyond the crater depth even in light solids, because of their low-energy per constituent atom and, in turn, do not create damage deeper in the sample. In the case of water ice targets, sputtering yields could be successfully predicted for fullerene energies in the range 5–120 keV, using a combination of short-time MD simulations and the newly developed “mesoscale energy deposition footprint” (MEDF) model.^{13,14} This model is based on fluid dynamics calculations, originally proposed to account for MeV particle interactions with solids.¹⁵ The MEDF model clearly shows the roles of both the size of the initially energized region and the cohesive binding energy of the substrate. Its adequateness to describe keV fullerene-induced sputtering also implies that, after a first step of fast energy deposition that is different under keV fullerene bombardment and MeV particle bombardment, the collective processes of molecular motion and emission are similar in the two energy deposition regimes. The assumptions underlying the MEDF model might break down for low projectile energies. Recently, another detailed study focused on the penetration of 0.1–80 keV fullerenes in a series of targets (Ar, Au, graphite, fullerite) demonstrated the pronounced range dependence on both the target atom bonding (cohesive energy) and the mass mismatch between the projectile and target atom constituents.¹⁶

From the viewpoint of materials scientists, molecular compounds that are solid at room-temperature constitute a very important class of samples for surface analysis, depth profiling, and imaging applications, whose specific response upon fullerene bombardement has not been studied yet. The list of target materials encompasses molecular (multi)layers (Langmuir–Blodgett, self-assembled), bulk polymers (synthetic or natural), electroactive molecules, polymer additives (antioxidants), and even pharmaceutical and biological samples (proteins, lipids, cells, tissues). In this contribution, we tackle the case of linear polymers, which form entangled networks of chains, with a naturally amorphous or semicrystalline structure. As a generic model system for simple polymers, chains without pendant groups, based on the polyethylene chemical structure, have been chosen. Beyond the description of the major effects observed in C₆₀-induced sputtering of polymers, this report focuses on secondary effects related to the molecular structure for compounds of the same nature and chemistry. Via a set of varying chain length, from 20 to 1000 CH₂/CH₃ units, we explore the effects of molecule size and entanglement on the desorption process. Because of the amorphous nature of the samples investigated in our simulations, possible effects of crystallinity are outside the scope of this study.

2. Computational Details

In order to describe the time-evolution of the investigated system at the microscopic level, Hamilton's equations of motion are numerically integrated over some time interval, providing us with the position and velocity of each particle at each time step.¹⁷ Forces among the atoms or particles in the system are derived from semiempirical interaction potentials whose careful choice constitutes the key of a realistic description of the studied mechanisms. In order to reduce the computational expense, certain atoms are grouped to form united atoms or particles. The advantages of such a coarse-grained approach are that there are fewer particles, the potentials are simpler thus quicker to calculate, and the fast H-vibration is eliminated which allows for a larger time step to be used in the integration.^{11,18} With this prescription, the large systems required to realistically describe keV fullerene interactions with organic solids can be treated within reasonable computation times. Validation of the model by comparison with an atomistic model using the many-body AIREBO potential was successfully achieved in the case of C₆₀ bombardment of benzene molecular solids.¹¹

The specifics of the computational cells used for the simulations of icosane (ICO) and polyethylene molecular samples (PE1, PE3, PE14; the numbers refer to the approximate molecular weights in kDa) are summarized in Table 1. As an example, the top and side views of the PE1 system are shown in Figure 1. This sample is a box containing $\sim 4 \times 10^5$ united atoms, forming $\sim 4 \times 10^3$ molecules, where each molecule is a string of 97 CH₂ particles of 14 amu and capped with 2 CH₃ particles of 15 amu. The amorphous icosane and polyethylene samples used in the sputtering simulations were generated as follows. First, a periodic unit cell containing a small number of molecules in an amorphous arrangement was designed at the atomistic level and relaxed using the Accelrys Cerius² software package. This basic cell was then coarse-grained by using the position of the corresponding carbon atoms for the coordinates of the CH₂ and CH₃ united atoms. Two hundred fifty-six of these cells were necessary to form the final ICO and PE3 samples and 405 cells were used to form the final PE1 and PE14 samples. The obtained solids, with the united atom positions defined as described above, were far from equilibrium within the potential set used for the sputtering simulations and several stages of heating and relaxation were necessary to reach an equilibrium configuration. With the chosen potentials, the final density of the relaxed icosane solid is 0.90 g/cm³. The calculated densities of the PE1, PE3, and PE14 samples are slightly higher (Table 1). Reported experimental values for the density of icosane at room-temperature vary between 0.79 and 0.93 g/cm³^{19,20} and for polyethylene, between 0.92 and 0.95 g/cm³.²¹

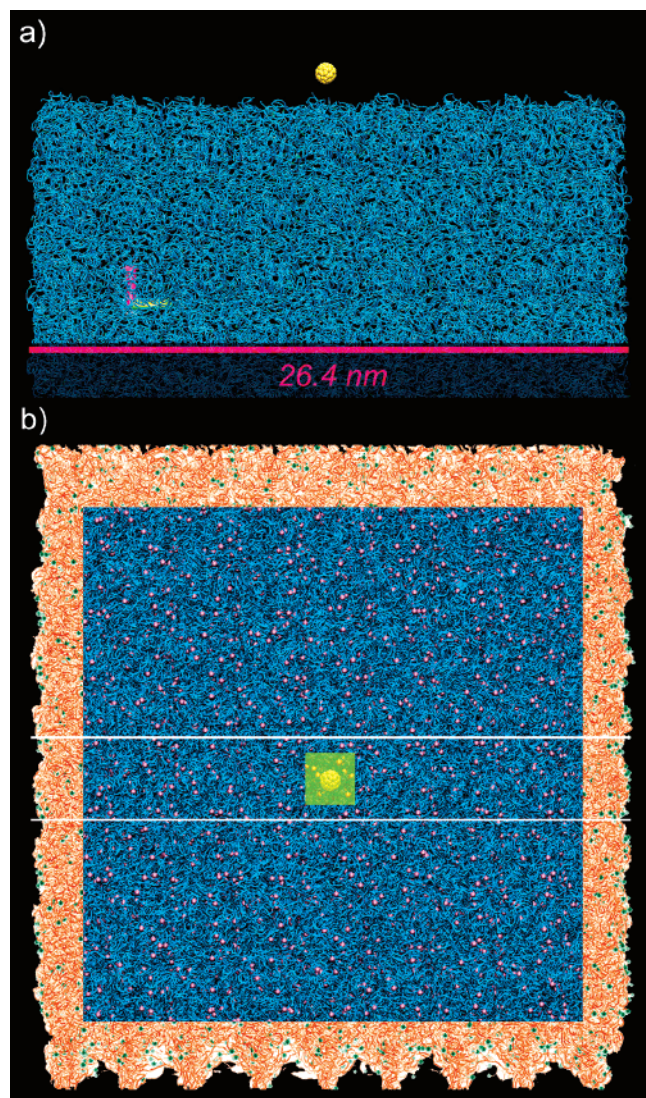


Figure 1. Sample cell for 5 keV C_{60} bombardment. (a) Side view of a slab vertically cut in the center of the PE1 sample (blue sticks) also showing the fullerene projectile (yellow). (b) Top view of the PE1 sample with the projectile impact zone (yellow square). The polymer chains are represented by blue sticks and the chain ends, by pink spheres. The orange region corresponds to the zone where stochastic and rigid boundaries are applied to avoid energy reflection. The white lines define the vertical section shown in (a).

In all of the sputtering calculations, a stochastic region at 0 K and a rigid layer are put on five sides of the samples in order to absorb the pressure waves induced by the C_{60} projectile.²²

In the coarse-grained model, a Lennard-Jones potential is used to describe the interactions of the particles located on different molecules. The values of ϵ and σ have been chosen from previous studies describing linear hydrocarbons.^{23,24} The intermolecular binding energies reported in Table 1 directly mirror the strength of these interactions in the relaxed samples. They were calculated as the difference between (i) the total potential energy of the relaxed sample and (ii) the potential energy of a single isolated molecule plus the energy of the entire sample without this molecule. The intermolecular binding energy per CH_2 particle varies between 0.098 and 0.078 eV with a trend of decreasing energy with increasing chain length. For the intramolecular interactions, the model must allow molecules to store internal energy up to the point when they dissociate. A Morse potential²⁵ between adjacent CH_2 and CH_3 particles has been chosen to account for the dissociating bond stretch term,

TABLE 2: Morse^a and Lennard-Jones^b Interaction Parameters

Morse	D_e (eV)	r_c (\AA)	α (\AA^{-1})	r_{cutoff} (\AA)
CH_2-CH_2				
1–2	3.6	1.53	2	5.0
1–3	0.01	2.52	2	5.0
CH_2-CH_3				
1–2	3.6	1.53	2	5.0
1–3	0.01	2.52	2	5.0
Lennard-Jones	ϵ (eV)	σ (\AA)	r_{cutoff} (\AA)	
$C-CH_2, C-CH_3$	0.0040	3.70	7.65	
CH_2-CH_2	0.0052	3.85	7.65	
CH_2-CH_3	0.0062	3.91	7.65	
CH_3-CH_3	0.0076	3.91	7.65	

^a The 1–2 interactions are defined as the nearest neighbor interactions and the 1–3 are the next nearest neighbor interactions. ^b A 12–6 Lennard-Jones potential is used.

with parameters that reflect the bond strength and equilibrium distance in linear hydrocarbons.^{23,24} With the chosen value of the parameter α , the curvature of the potential energy function at equilibrium ($2^*D_e*\alpha^2$) is very close to that obtained by Balasubramanian et al. for the harmonic bond stretch term of such hydrocarbons.²⁴ The other interactions are between CH_x particles separated by one CH_x particle, which are modeled by a Morse potential with a small well depth.¹¹ This pair potential allows the particles to interact if the molecule is dissociated and also provides an equilibrium configuration of the sample in which the molecules adopt the appropriate zigzag shape. This type of interaction has been preferred to an angle bend term that does not allow for dissociation and is therefore limiting for sputtering simulations. For CH_x particles of a molecule that are separated by two or more particles, a Lennard-Jones potential with the same parameters as the one used for intermolecular interactions is used. The Morse and Lennard-Jones potential parameters are summarized in Table 2. In all of the simulations, the AIREBO potential is used to describe the C–C interaction of the C_{60} projectile.²⁶ A weak Lennard–Jones potential is used between the C atoms of the fullerene and the CH_x particles of the molecular sample (see Table 2).

3. Results and Discussion

In the first part of the results, the energy transfer of the projectile to the polymeric medium and the mesoscopic process of crater and rim formation are explored in detail (sections 3.1 and 3.2). In the remainder of the article, we focus on the sputtering of molecules and fragments (sections 3.3 and 3.4). An important section is devoted to the emission from icosane, where the large number of sputtered molecules allows us to obtain statistically significant distributions for the velocities, energies, and depths of origin. Then, the conditions for the emission of large intact molecules from an amorphous polymer upon kiloelectronvolt fullerene impact are analyzed. The last section (3.5) investigates the influence of the projectile energy on crater formation and molecular emission, including comparisons with recent experiments.

3.1. Overview of the Sputtering Process. The penetration of a 5 keV fullerene projectile in a polyethylene solid (PE14) is illustrated in Figure 2. At 100 fs, the projectile has already split into its constituent atoms but they keep acting in a collective manner, pushing ahead a hemispherical front of target particles that becomes clearly visible at 600 fs (white arrows). Also, at that moment, a bifurcation of the overall motion is visible, with about half of the C atoms penetrating deeper inside the forming

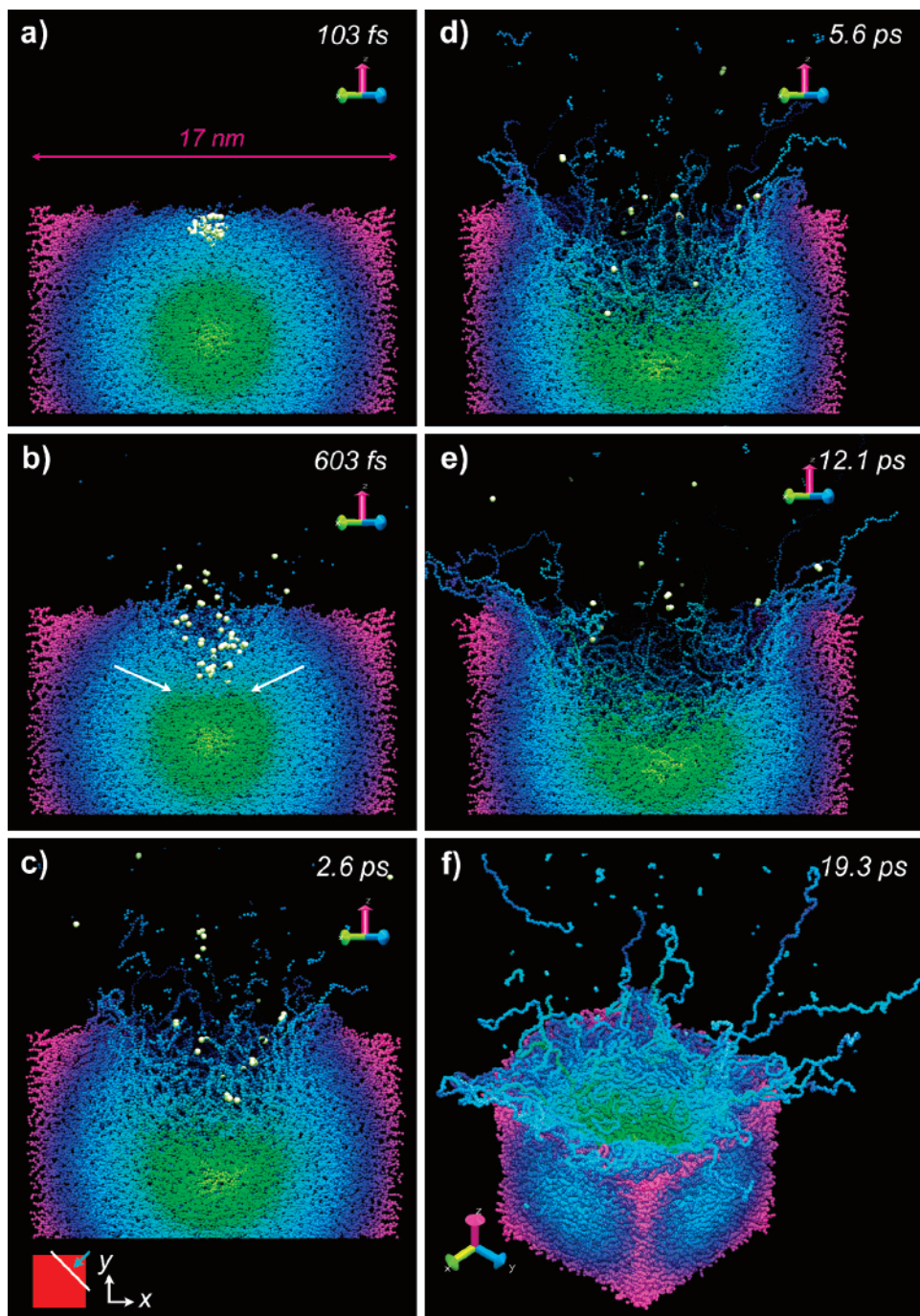


Figure 2. Time-evolution of the interaction between a fullerene projectile and PE14. (a–e) Side views of a cube (120 Å side) vertically sectioned in order to show the inside of the crater (angle of view signified by the blue arrow in the inset of panel c). Color coding is a radial function of the position of the particles in the sample before impact (from green to purple from the geometric center to the edges of the cube). The projectile atoms are shown as white spheres. (f) Orthogonal perspective view of the crater and dangling polymer chains at 19.3 ps.

crater and the other half being reflected toward the gas phase. The “splitting plane” is located at ~20 Å under the sample surface.¹³ Some of the target material (especially small fragments) follows the upward motion and is emitted at that time. At 2.5 ps, the polymer chains that were first compressed in front of the projectile expand upward, in the void of the forming crater. The crater reaches its maximum size before 12 ps. Between 2.6 and 12 ps, one observes a flux of polymer material expanding outward from the walls of the forming crater. Polymer chains unfold into the vacuum, some of them being ejected while others redeposit to form the crater rim. Many long chain segments are still dangling above the surface at 19–20 ps.

The behavior observed in Figure 1 for PE14 is representative of a trend that applies for all of the samples, with the exception of ICO, where the chains are very short. Desorption from an ICO sample has been described in ref 18. The energy transfer and crater formation processes are similar, but after 20 ps, molecules are either desorbed and in the gas phase or they are settled in the solid. In contrast, many of the long chains of PE1, PE3, and PE14 samples that start desorbing because of their translational energy, do not have a sufficient quantity of internal energy to cause the bond-scission or break the entanglement that would free themselves from the surface. Specific effects related to the molecular structure of the samples will be pointed out later in this article.

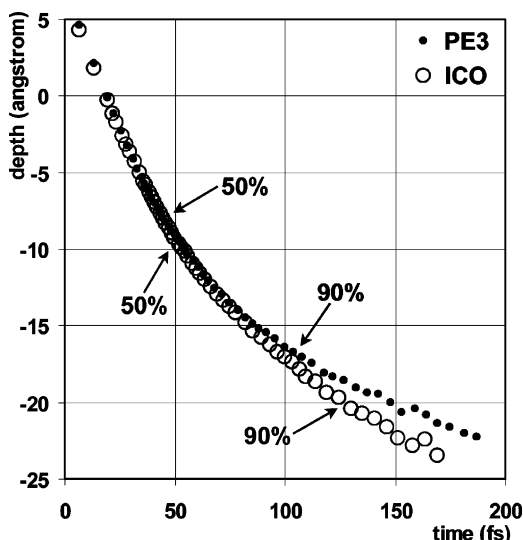


Figure 3. Penetration depth of the projectile center-of-mass as a function of time for ICO and PE3 samples. The percentages indicate the fraction of the projectile energy that has been already transferred to the target atoms.

3.2. Projectile Penetration, Crater Formation, and Material Redeposition. As indicated by the snapshots of the molecular dynamics (Figure 2), 5 keV fullerene projectiles do not penetrate deep into the polymeric solid. Figure 3 shows the position of the center-of-mass of the projectile as a function of time for ICO and PE3 samples, over a time range in which the vast majority of the C atoms of the fullerene are still moving downward in a somewhat correlated manner (i.e., before the aforementioned momentum bifurcation). Within 100 fs, the fullerene has transferred approximately 90% of its energy to the organic medium. The tracks of the projectiles merge for the different samples down to a depth of 10–15 Å and start slightly diverging afterward, with the projectile penetrating deeper in the case of the icosane sample. The percentage of the projectile energy transferred to the sample indicates that C_{60} releases its energy slightly but significantly slower and deeper in the short chain solid than in the higher molecular weight polymer. The depth of penetration for a 90% energy transfer is 20 Å for ICO and 17 Å for PE3.

After the impact and the transfer of the projectile energy to the target atoms (100 fs), the energy diffuses radially from the center of the energized hemisphere. The situations at 2 ps (top frames) and 20 ps (bottom frames) are shown in Figure 4 for ICO and PE1 samples. Only particles with more than 8×10^{-3} eV of kinetic energy (~ 100 K) are shown for clarity. Even though both samples show a quite similar, radial energy distribution at 2 ps, especially in the high-energy volume directly surrounding the impact (~ 50 Å radius), the density of energy in the outer region, from 50 to 100 Å radius, is comparatively larger for the ICO sample (significantly more particles with energies in the range 0.01–0.03 eV). After 20 ps, when the crater is fully formed, the energy has diffused outward and few particles in the solid have more than 0.05 eV of kinetic energy, which is close to the cohesive energy per particle in the solid. Only fragments and molecules hovering above the solid-phase retain a larger quantity of energy.

Material-related differences in the energy transfer process are mirrored by the size of the crater. In Figure 5, the shapes of the craters formed after 20 ps in ICO and PE3 samples are superimposed for comparison. Characteristic values (diameter, depth) describing the crater sizes are listed in Table 3 for all of the investigated samples. It is clear from these values that

icosane stands out of the sample series, whereas the three other polymeric solids (PE1, PE3, and PE14) exhibit comparable values with respect to the crater size. The width of the rim surrounding the crater is also larger for icosane (~ 40 Å) than for the other systems (~ 30 Å). To help us understand the formation of the rim, Figure 6 tracks the origin of the involved matter back to the situation of the sample before impact. The chosen polymer sample is PE3, but the mechanism is qualitatively similar for all of the studied targets. Figure 6a–c shows top views of the dynamics only including the material that has been ejected in the gas phase over the first 20 ps or forms the crater rim at 20 ps (above the original surface plane). The polymeric material is colored radially from the impact point (cyan) to the periphery (red). With this formalism, one observes that the polymer chains initially located in a 25 Å radius around the impact point (cyan) are almost totally ejected, whereas the outer ring (blue-purple) of molecules gradually expands with time up to the end of the trajectory. At 20 ps, many of these polymer chains have re-deposited on the surrounding surface, forming the crater rim, whereas some others are still dangling into the vacuum. The top views of Figure 6a–c, together with the combined side views of Figure 6d, show that the most peripheral polymer chains (red) actually “slide” or “creep” over the surrounding material, moving outward by less than 20 Å, whereas the intermediate ring (blue-purple) displays a wider movement (white arrow) that finally brings the corresponding molecules over those originating from the extreme periphery (red). Some of the molecules entrained in this sweeping movement are ejected intact and others remain bound to the solid phase. Another important observation arises from the examination of the side view of the corresponding material before impact. Although the full crater depth at 20 ps is close to 50 Å (Table 3), the material that is sputtered and/or redeposited in the rim comes from a maximum depth that does not exceed 30 Å. In fact, the volume of matter located between 30 and 50 Å depth before impact actually moves downward upon compression during the process, creating a region of increased density at the bottom of the crater. Trajectories computed over 50 ps show that the level of the crater bottom does not change between 20 and 50 ps, which indicates that the higher density region does not relax by regaining volume over this time range. The same observation holds for simulations of C_{60} bombardment of water ice¹³ and benzene solids.

3.3. Emission of Molecules and Fragments. The formation processes of sputtered fragments and molecules is important for SIMS analysis. In this section, the emission characteristics (origin, velocity, kinetic energy) and mechanisms of fragments and relatively small molecules from a non-entangled solid (ICO) are investigated. The conditions of emission of a large intact molecule from an entangled medium are explored in the following section.

In the case of ICO samples, the sputtered flux consists of a mix of fragmented and intact molecules. As shown in Table 3, an average number of 78 molecules are ejected for each fullerene impact. The statistics collected over 9 trajectories are therefore sufficient to extract distributions (depth of origin, energy, velocity) that realistically describe the properties of the desorbed molecule flux. The distributions of Figure 7a show the depth of origin of intact ICO molecules together with that of CH_2 fragments (one single particle in the model). In contrast with experimental²⁷ and theoretical^{28,29} results obtained upon atomic bombardment of organic samples, the origin depth distributions of (atomic) fragments and molecules are not strongly different upon C_{60} bombardment. For a 5 keV impact energy, all of the

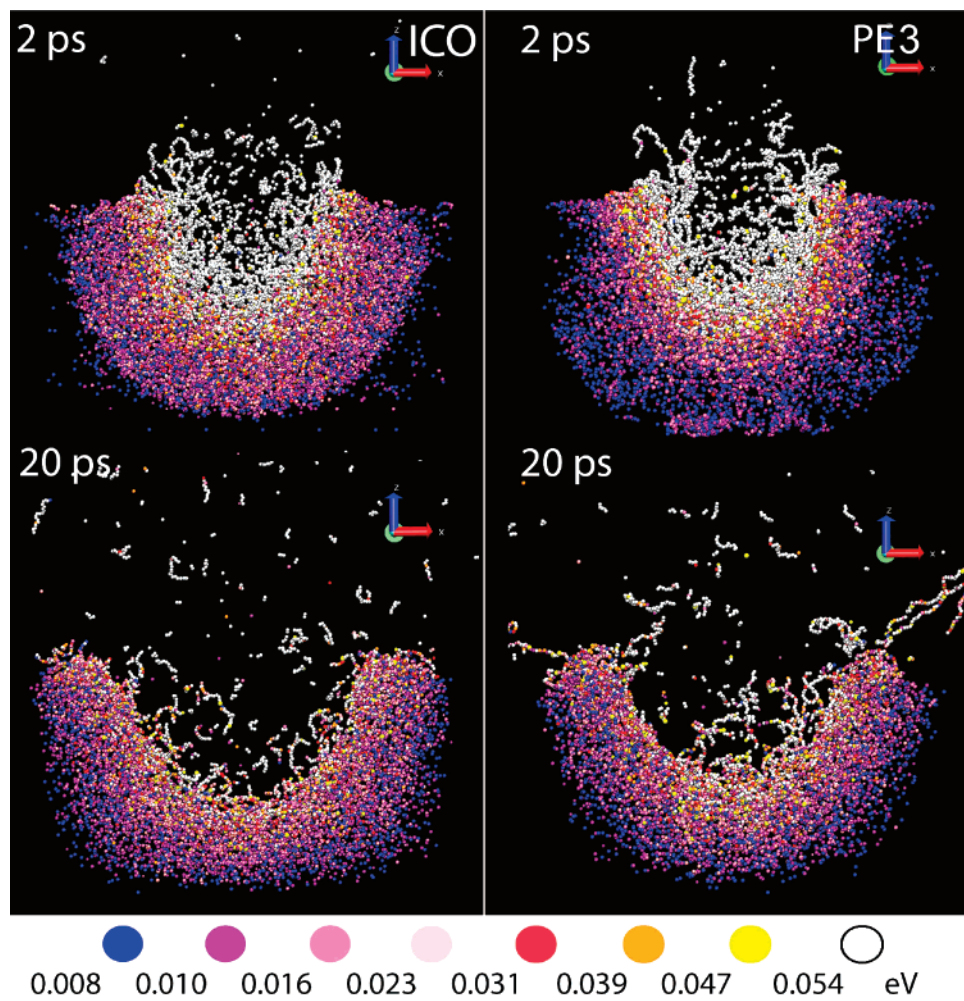


Figure 4. Kinetic energy of the atoms in a 30 Å thick vertical section of ICO and PE3 samples, at 2 and 20 ps after the impact of a 5 keV fullerene. The atoms are colored from blue to white according to their energy. Only atoms with more than 0.008 eV of kinetic energy are represented.

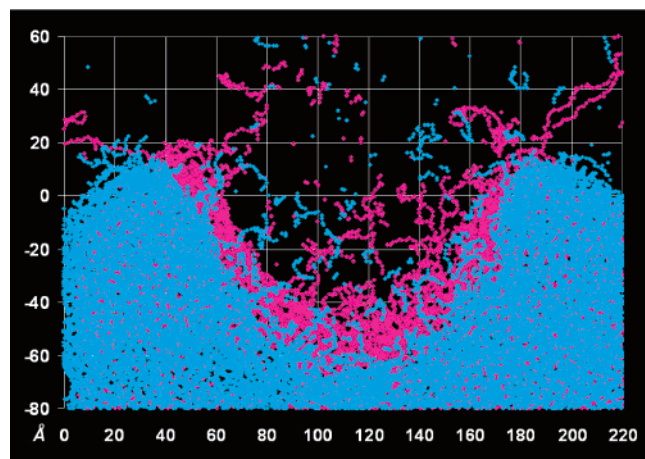


Figure 5. Overlay of two vertical sections of ICO (blue) and PE3 (purple) samples showing the shapes of the craters after 20 ps.

sputtered species come from the maximum depth of 30 Å below the surface. Slight differences in the distribution shapes and maximums show that CH₂ fragments are predominantly sputtered from a depth of 10–14 Å, whereas intact ICO molecules are more surface-specific, with a maximum, plateau emission extending from 3 to 12 Å. Figure 7b,c illustrates the origin of the same species via a geometric representation, with top and side views showing the point of origin of their center-of-mass in the undisturbed sample. These views provide us with the

TABLE 3: Influence of the Sample Nature on Crater Formation and Sputtering upon 5 keV C₆₀ Bombardment

sample	ICO	PE1	PE3	PE14
crater Ø (Å)	122	102	97	95
crater+rim Ø (Å)	207	161	162	161
crater depth (Å)	57	49	47	47
sputtered mass (Da)	31590 ^a	25930 ^a	19960 ^a	14590 ^b
number of molecules	78	6.6	0.1 ^c	0

^a These values are an average over 9 (ICO, PE3) or 5 (PE1) trajectories. In all cases, the standard deviation was less than 10%.

^b This value has been calculated from a single trajectory. ^c Only one PE3 molecule was emitted intact over 9 trajectories.

information missing in Figure 7a. They show that the CH₂ fragments originate from an almost perfectly spherical region of the sample surface, with a diameter of ~35 Å. This volume corresponds to the high-energy density region formed over the first 200 fs of the projectile surface interaction, when most of the bond-scissions occur in the sample.¹⁸ In contrast, intact molecules desorb from the periphery of a wider hemispherical region. The maximum diameter of this annular volume, close to ~90 Å, is located at the sample–vacuum interface, which explains the distribution maximum/plateau of Figure 7a.

The flux of intact molecules sputtered from the peripheral region is further characterized by their velocity vectors. In Figure 8, the velocity vectors of ICO molecules are represented by their projection on the XY and XZ planes, with their origin positioned at the center-of-mass of the molecule prior to impact.

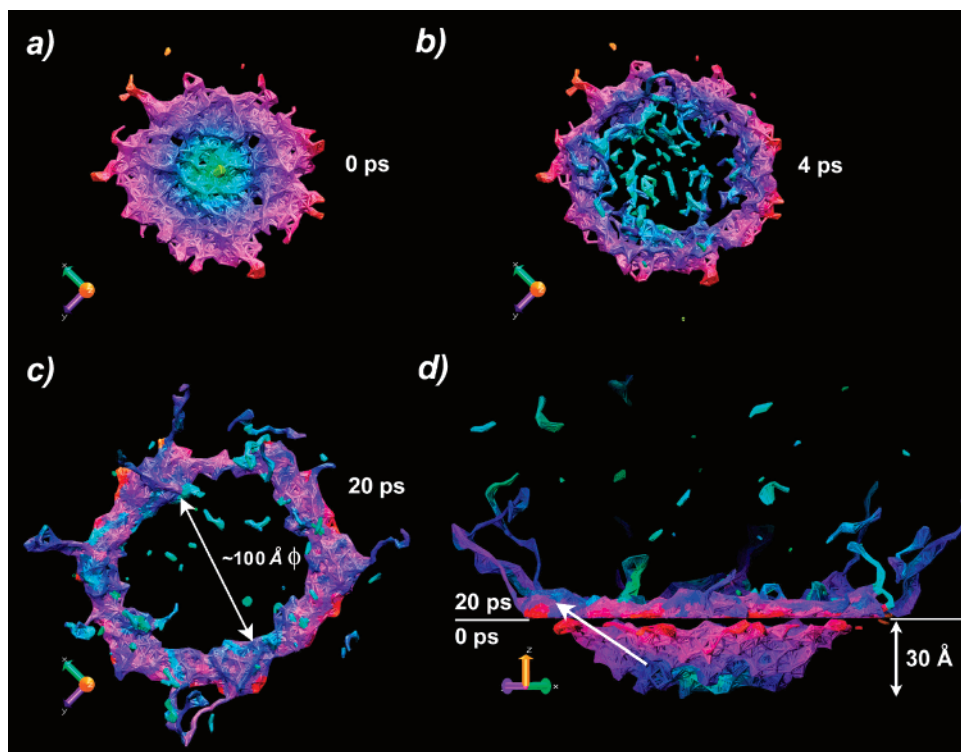


Figure 6. Five keV C₆₀ bombardment of PE3. (a–c) Top views at different times only showing the material that ends up above the surface plane at the end of the trajectory (20 ps). This representation provides a direct indication of the origin of the material that is sputtered and/or redeposited in the rim. Color coding is from cyan to red from the center (impact point) to the edges of the crater. (d) Side view of the same material at 0 and 20 ps. The surface plane is signified by the white line.

The results indicate the overall correlation between the relative position of the molecules with respect to the impact point (Figure 8a) and the direction of their velocity vector as well as the predominant upward component in the velocity of the ejected molecules (Figure 8b).

Another effect that might be less obvious is that molecules desorbed from the surface have, on average, larger velocities than molecules emitted from deeper in the sample. This effect is shown by the total magnitudes and by the vertical components of the velocity vectors of sputtered icosane molecules, which are plotted as a function of the depth of origin in Figure 9a. Molecules sputtered from the top 15 Å exhibit an average Z velocity that is greater than 500 m/s, with peaks above 2000 m/s, whereas the majority of molecules originating from a deeper plane have velocity distributions that peak around 500 m/s.

The dependence of the velocity on the mass of the sputtered species is very similar for the 4 investigated polymer targets. It is exemplified in Figure 9b with the case of icosane. The average velocity decreases in a nonlinear fashion over the range of sputtered masses. Typical velocities for CH₂ species are around 3000 m/s, whereas large clusters (ICO) or molecular fragments (PE1, PE3, and PE14) above 1 kDa are essentially slower than 1000 m/s. The full lines show the mass-dependence of the average velocity $\langle v \rangle$ that would be obtained for Maxwell–Boltzmann distributions of particles with the same mass. The very high temperatures corresponding to these velocities indicate that the ejected molecules and fragments arise from a largely superheated nanovolume.

The velocity plots of Figures 8 and 9 confirm the collective, mesoscopic nature of the ejection process. A dependence of the axial velocity on the depth of origin is also observed in laser ablation of organic samples³⁰ and sputtering of rare gases³¹ and water ice.³² However, the dependence of the velocities on the mass of the sputtered species observed in Figure 9b does not

suggest the entrainment effect sometimes observed in laser ablation. Even though the scale of the process was much more limited, a pronounced mass-dependence of the velocities was also found upon 500 eV Ar bombardment of kilodalton polystyrene oligomers embedded in a low-molecular weight matrix.²⁹ The mass-dependence of the velocities in Figure 9b reminds thermal evaporation but the out-of-equilibrium nature of the entire process, the high-energy density in the track core and associated energy gradient (Figure 4), the large translational temperatures of the emitted species (Figure 9b), and the flow of material in the crater (Figure 6) point to a more complex process. The average velocities mirror the temporal and spatial evolution of the dynamics, in which single particles and small fragments are mostly desorbed at early times from the energized region surrounding the projectile track, whereas larger species desorb at later times from the periphery.

In parallel to their velocity, the translational energy of secondary species is a quantity that can be directly measured in instruments equipped with electrostatic sectors or mirrors. The energy distributions of CH₂ fragments and intact molecules sputtered from icosane are illustrated in Figure 10. Both distributions peak in the range 0–1 eV, but the maximum energy of the CH₂ distribution is significantly larger than that of intact molecules and the distribution is markedly wider between 0 and 3 eV. Nevertheless, the distribution corresponding to a single particle (CH₂) in the model does not extend beyond 10 eV. This observation is in contrast with the case of kiloelectronvolt atomic bombardment of solid inorganic and organic samples.³³ The comparatively low average kinetic energy of small particles ejected under C₆₀ bombardment mirrors the low-energy per constituent atom in the fullerene projectile and the nonlinear cascade-type of the emission process. The energy distribution of ICO molecules desorbed from a molecular solid can be compared to the case of molecules (benzene, polystyrene)

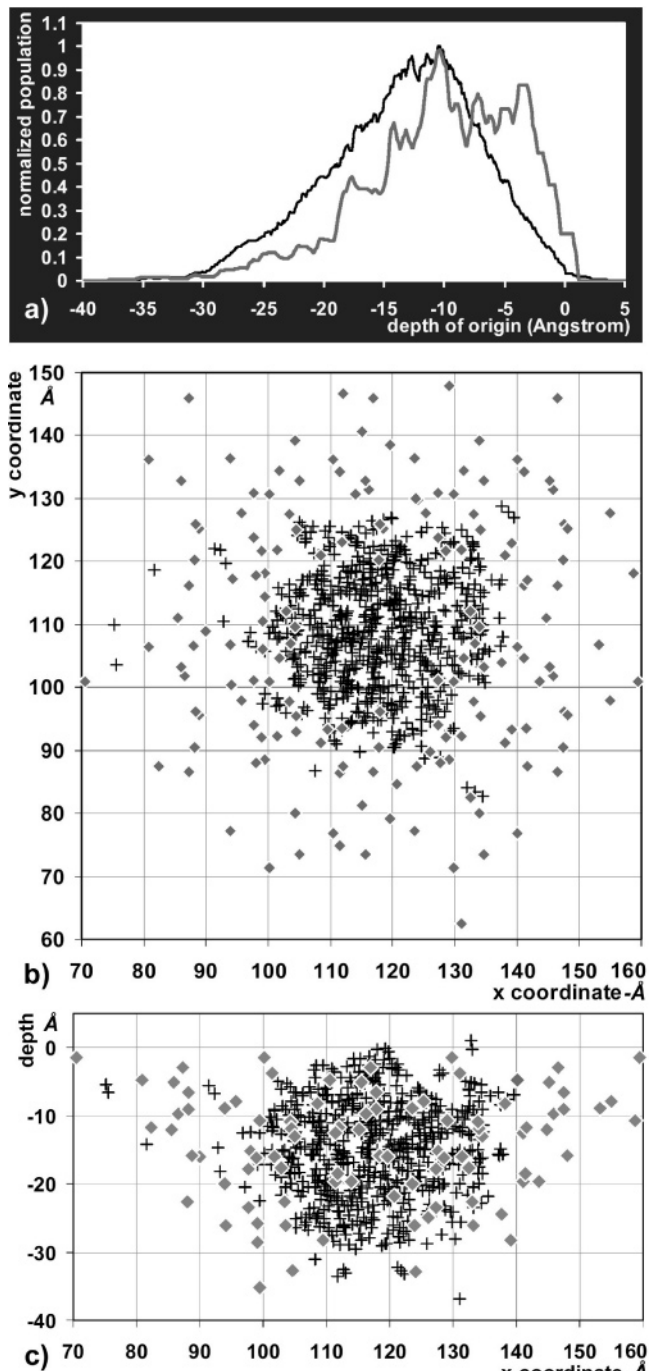


Figure 7. Origin of the sputtered species upon 5 keV C₆₀ bombardment of ICO. (a) Depth distributions of the sputtered CH₂ fragments and entire molecules. (b) Top and (c) side views plotting the center-of-mass of the CH₂ fragments (crosses) and entire molecules (diamonds) before their emission.

emitted from an overlayer on metal by C₆₀ projectiles.³⁴ The energy distribution of icosane sputtered from the bulk is very similar to the one calculated for benzene (low binding energy) and much narrower than the one of polystyrene (higher binding energy). Because of its intermediate size, one would expect the distribution of icosane ejected from a metallic solid to be broader than that of benzene, as an effect of its larger binding energy. With this assumption, one can speculate that the average translational energy of ICO molecules sputtered by C₆₀ from the bulk might be lower than that of molecules sputtered from an overlayer on metal. On the other hand, the calculated distribution of ICO molecules (Figure 10) is close

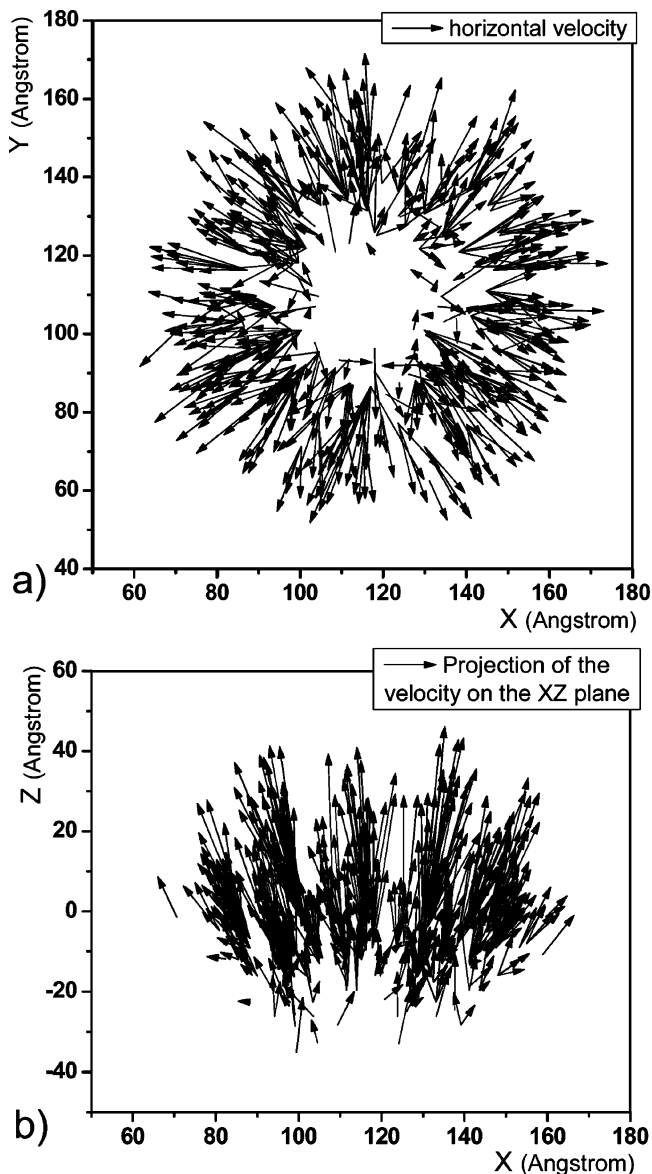


Figure 8. Velocity vectors of the molecules ejected upon 5 keV C₆₀ bombardment of ICO (calculated at 20 ps). The origin of the vectors are placed at the position of the center-of-mass of the molecules before impact. (a) Top view. (b) Side view.

(slightly wider) to the one of polystyrene oligomers sputtered from the bulk by Ar projectiles and the binding energy of the two molecules is similar (~ 2 eV in the bulk).³⁵ Therefore, the type of projectile (monatomic or polyatomic) does not seem to have a strong influence on the translational energies of molecules sputtered from bulk organic samples.

The much narrower energy distribution observed for single particles (atoms) upon C₆₀ bombardment, in comparison with atomic projectiles, is a general trend also valid for metals.³⁶ These lower kinetic energies might be instrumental in explaining the experimental observation that the yields of atomic secondary ions are significantly less enhanced by C₆₀ than the yields of molecular ions (for all types of materials). Two effects might actually play in the same direction of lowering the ionization probability of atomic species. First, the direct ejection of an electron from the atom upon close encounter should be less probable because of the very limited energy of each C constituent of the fullerene. Second, the lower velocity of the atoms leaving the surface should result in their more efficient reneutralization.

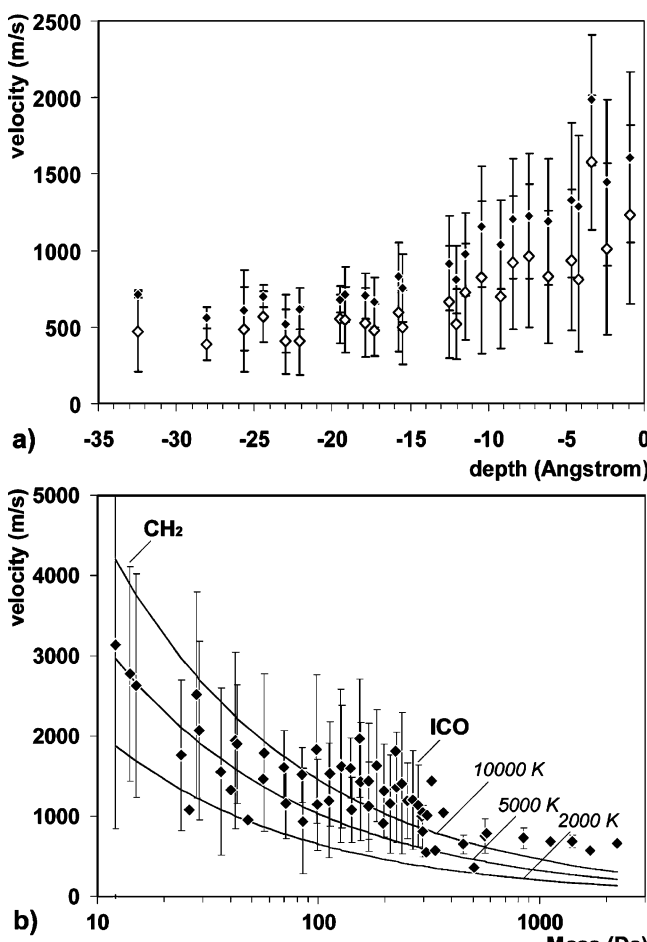


Figure 9. Final velocity of the species ejected upon 5 keV C_{60} bombardment of ICO. (a) Average total velocity (full diamonds) and vertical component (z) of the velocity vectors (open diamonds) of intact ICO molecules plotted as a function of their depth of origin in the sample. (b) Average total velocity of all the species sputtered from ICO plotted as a function of mass. The gray lines signify the calculated average velocities for Maxwell–Boltzmann distributions (at 2000, 5000, and 10 000 K) of particles with the same masses. In both graphs, the vertical bars indicate the standard deviation with respect to the average.

3.4. Large Molecules: Mechanisms of Fragmentation and Intact Ejection. As shown in Table 3, increasing the molecular weight of the polymer chains forming the sample affects the sputtering process. When going from ICO (282 Da) to PE14 samples (14 kDa), the crater becomes significantly smaller and the amount of ejected material decreases by a factor of 2. Part of the sputtered mass reduction can be attributed to the smaller size of the displaced volume (crater size). Another effect influencing the total sputtered mass is directly related to the size and structure of the chains. Although smaller chains can be easily detached from the surrounding organic medium and ejected, larger chain segments tend to remain bonded to the solid by covalent binding and entanglement. Therefore, in contrast to other sets of materials,¹⁶ the sputtered mass decrease cannot be directly explained by the strength of the intermolecular forces which, ratioed to the number of particles per molecule, are quite similar for all of the samples of this study (they actually decrease slightly with molecular mass, see Table 1). Instead, structural parameters of chain length and entanglement dominate.

It has been shown that, under 5 keV C_{60} bombardment, extensive (primary) damage in the sample via bond-scissions is geometrically limited to a nanosphere that is about 15–20 Å

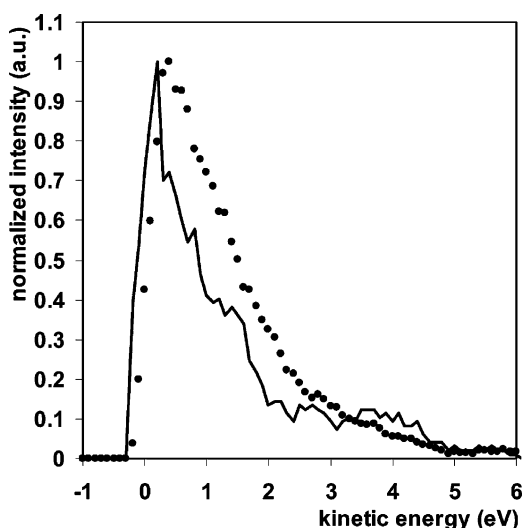


Figure 10. Kinetic energy distributions of the sputtered CH_2 fragments (circles) and intact molecules (line) under 5 keV C_{60} bombardment of ICO. To obtain these curves, the raw data were convoluted with a 0.5 eV width square function, which induced a slight broadening of the distributions (intensity below 0 eV). The resulting distributions were peak normalized.

in radius. Secondary damage involving material displacement and relocation as well as other changes of the surface properties (surface topography, density of the material), however, extend to a much larger hemispherical volume that is well defined by the metrics of Table 3. Secondary ion mass spectrometry is particularly sensitive to the primary damage, i.e., bond-scissions, because it directly affects the integrity of the molecules and, in turn, the peak patterns of the mass spectra. In a preliminary study focused on projectile-induced damage in icosane, it was already shown that one single 5 keV fullerene creates about 300 radicals in the solid, which corresponded to 44 broken molecules, slightly more than half the number of molecules ejected intact in the same event.¹⁸ Because of their small size, the volume of damaged icosane molecules is similar to the volume where bond-scissions occurs. The situation is different for significantly longer oligomer chains such as PE3 or PE14 that may extend over distances comparable or larger than the radius of the damaged volume. This effect is illustrated in Figure 11a by a top view of the PE3 molecules that underwent bond-scissions in one of the calculated trajectories. In that vignette from the MD simulations, the radius of the dashed circle, indicative of the crater size, is ~50 Å, and one notices that some of the damaged molecules even extend beyond that distance. It is also suggested by Figure 11a that, in addition to their molecular weight, the geometric structure of the target molecules plays an important role in the extension of damage induced in the sample surface. Consider for example a molecule that contains the number of atoms found in the primary damage region. If this molecule is compact and nonentangled with the surrounding molecules (e.g., a crystallized protein), the impinging projectile might only damage that one molecule upon impact. At the other extreme, if molecules with the same size are very extended, either linearly aligned in a crystal or swollen by a number of other molecules in a strongly entangled polymeric medium, the projectile will always damage many molecules at the time and, in turn, degrade a much larger surface area. A metric that can be used to quantify the spatial extension of the molecule in the surface is the gyration radius. In this article, the horizontal gyration radius is defined by the equation

$$R_{gh}^2 = \{ \sum [(x_i - x_{\text{mean}})^2 + (y_i - y_{\text{mean}})^2] \} / N$$

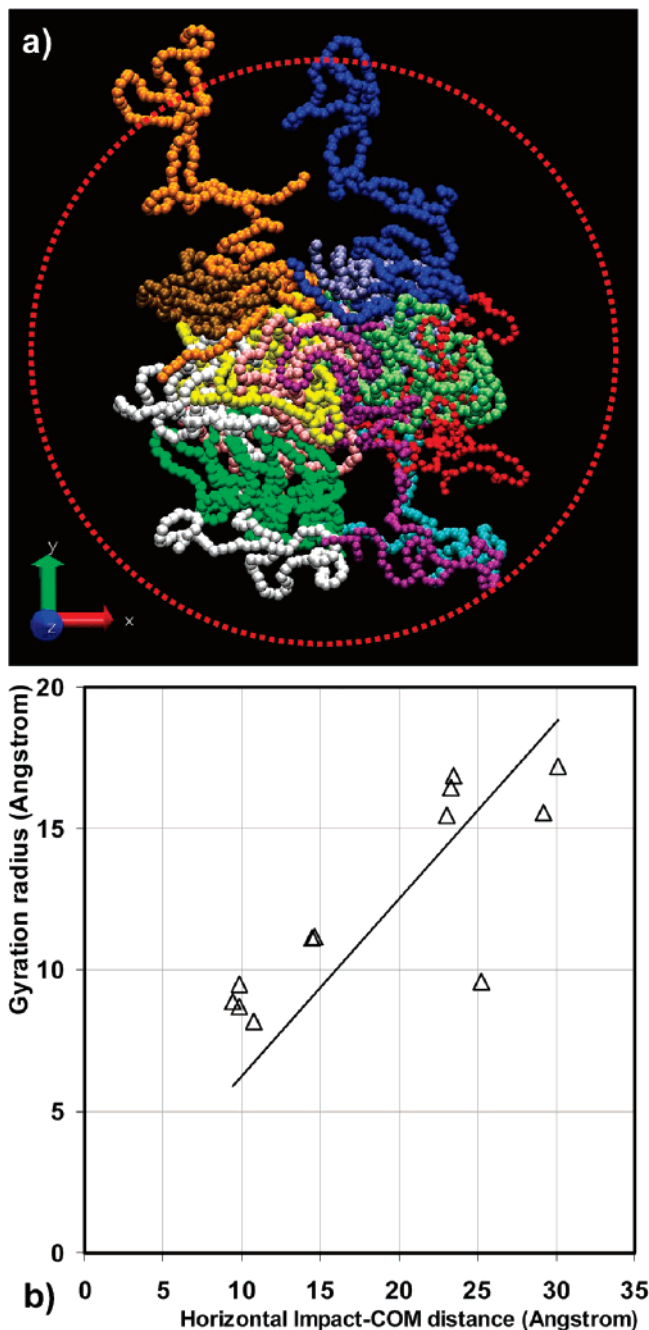


Figure 11. Fragmentation of molecules under 5 keV C_{60} bombardment of PE3. (a) Top view before impact ($t = 0$ fs) of the molecules that undergo single or multiple bond-scissions in a selected trajectory (one color per molecule). The red circle signifies the size of the final crater. (b) Horizontal gyration radius before impact ($t = 0$ fs) of the fragmented molecules plotted as a function of the distance between the center-of-mass of the molecules and the impact point.

where N is the number of particles in the molecule, x_i and y_i , the horizontal coordinates of the i th particle and x_{mean} and y_{mean} , the horizontal coordinates of the mean position of the particles. The values of R_{gh} are plotted in Figure 11b for damaged PE3 molecules, versus the distance of their center-of-mass with respect to the impact point. The range of gyration radius of the considered PE3 molecules (calculated at $t = 0$ fs), from 8 to 18 Å, simply provide a quantitative measure to the visual observation that, despite their identical molecular weight, some molecules extend over a larger surface area than others. The overall correlation between gyration radius and impact to center-of-mass distances for broken molecules demonstrates that, more

than the actual molecular weight of the molecules, it is their lateral spread that eventually defines the size of the damaged area. In other words, molecules that cover a larger surface area in the pristine sample have a larger probability of undergoing bond-scissions upon impact than molecules with a smaller spatial extension. A correlation between the characteristic size of the species of interest and their damage area or cross-section was reported for smaller polymer fragments in a previous article.³⁷

The absence of bond-scission in the molecules upon impact of the projectile constitutes an obvious requirement for the emission of intact species. One may wonder what are the other conditions that permit or limit the emission of molecules upon kiloelectronvolt C_{60} bombardment of polymers such as the PE samples of this study. Table 3 shows that the number of molecules sputtered intact decreases dramatically with increasing molecular size. Over a series of nine calculated trajectories, only one PE3 molecule (3.5 kDa) is desorbed as a whole. This observation is partly explained by the size-dependent damage effect described before. However, another important effect also comes into play, which relates to the size of the displaced volume or the radius of the forming crater. In order to understand the role of the crater size on intact molecule ejection, it is informative to analyze the only trajectory in which a PE3 molecule was desorbed without fragmentation. Figure 12 shows snapshots illustrating the time-evolution of that trajectory. For clarity, only the molecules that are damaged upon impact and the molecule to be desorbed intact are represented, with a different color for each molecule. First, the images of the situation at 0 and 2 ps make it clear that all of the molecules that were intersecting the ~30–40 Å sphere of primary damage, but one (in white), are actually broken as a result of the projectile impact. The process is stochastic, and from the set of calculated trajectories, the survival of molecules directly surrounding the impact point appears improbable. The top and side views of the original situation of the surviving molecule in this trajectory (Figure 12f,g), significantly distant from the impact point, help us understand why it could escape destruction. With time, the white molecule slowly unfolds into the gas phase, as a part of the overall upward motion affecting the molecules in the top ~20–30 Å of the disturbed volume. In contrast, the (broken) blue molecule in the depth of the crater, because of its original situation below the splitting plane described in Figure 2, mostly receives downward momentum in the beginning of the interaction and, therefore, never ejects. The momentum variation across the depth of the crater also influences the white molecule. It is obvious after 6 ps, when a large portion of the molecule is already above the surface while the lower part has barely moved yet. As a matter of fact, our results indicate that it is the depth and lateral dependence of the momentum amplitude and direction that cause the complete unfolding of most molecules and large chain segments. This variation of particle momentum across the molecule directly translates in terms of internal energy of the molecules. The white molecule in Figure 12 eventually ejects because it comes from a region of the surface where the momentum is predominantly upward-directed and sufficiently large to cause desorption. In contrast, the molecules that were originally surrounding the colored molecules in Figure 12a, not shown, do not receive enough momentum to detach from the solid and desorb. They are either dangling in the vacuum or forming the crater rim at the end of the trajectory.

Our analysis shows that several criterias must be met for a molecule to be sputtered intact upon fullerene cluster bombardment. (i) No bond should be broken by the projectile, i.e., the molecule should overlap as little as possible with the high-energy

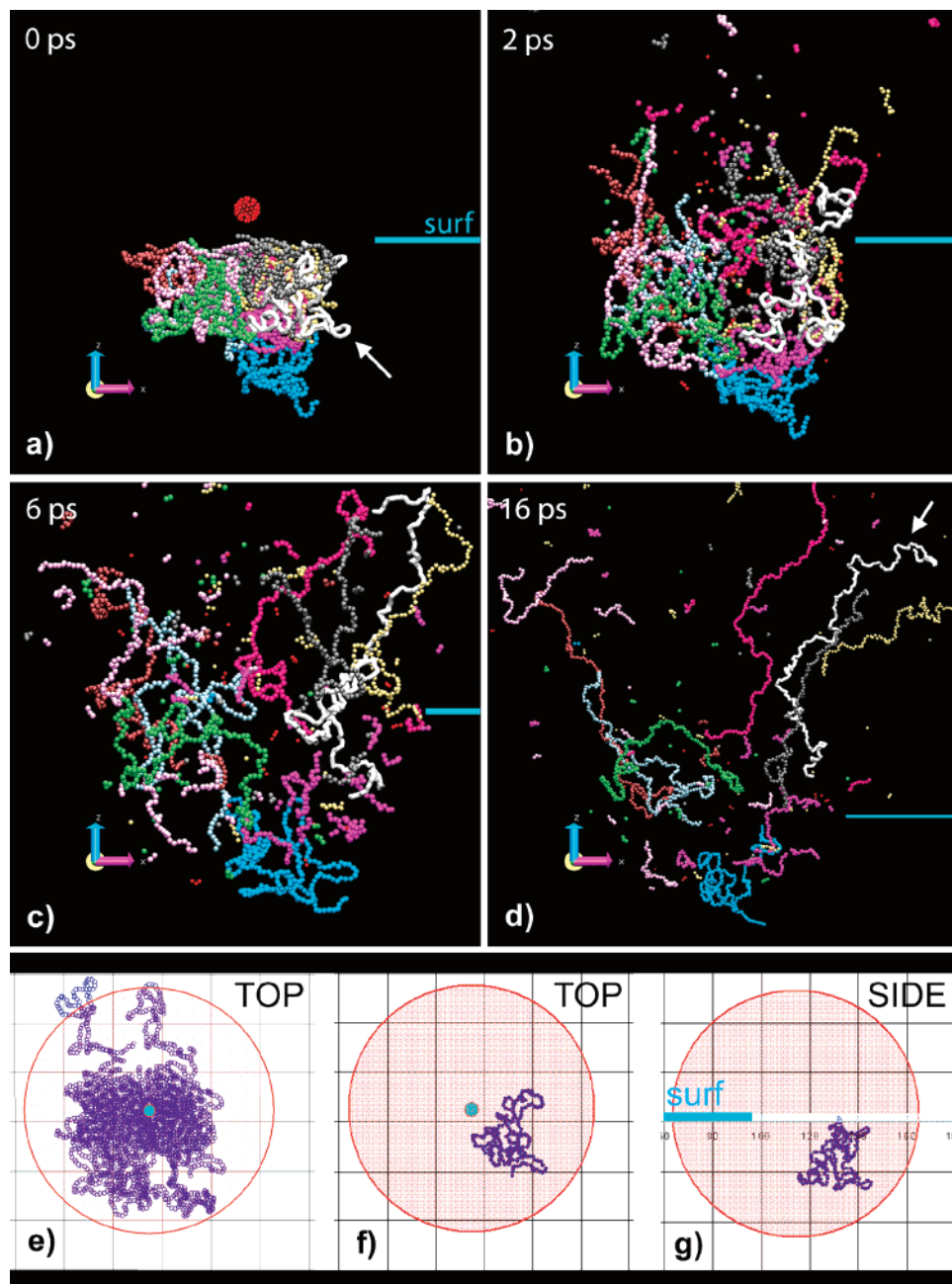


Figure 12. Emission of an intact molecule under 5 keV C_{60} bombardment of PE3. (a–d) Side views of the time-evolution of the trajectory only showing the fragmented molecules (colored spheres, one color per molecule) and the molecule that is ejected intact (white sticks). The sky blue line indicates the level of the surface plane. (e) Top view of the situation of the fragmented molecules before impact. (f and g) Top and side views of the initial situation of the molecule desorbed without fragmentation. The red disk signifies the extent of the crater at the end of the trajectory.

core of the projectile track. (ii) The molecule should be entirely included in the displaced volume (the crater) before emission. (iii) For 5 keV C_{60} bombardment, it should sit in the top 30 Å of the sample, essentially in the zone where the momentum of the target atoms is upward directed around 0.5–1 ps after impact. Corollaries of our observations are that large or strongly entangled molecules are less likely to be ejected intact and that the internal energy of the sputtered molecules depends on both their spatial spreading and their initial position with respect to the impact point. The effect of the projectile energy will be discussed in the next section.

3.5. Influence of the Projectile Energy. For the PE1 sample, trajectories were calculated with varying projectile energies, in the range 1–10 keV. The statistics concerning crater sizes, displaced material, and sputtered species are listed in Table 4. Both the crater diameter and the crater depth grow nonlinearly

TABLE 4: Influence of the Projectile Energy on the Sputtering Characteristics of PE1 Samples^a

C_{60} energy	1 keV	2 keV	5 keV	10 keV
crater \varnothing (Å)	56	76	102	124
crater+rim \varnothing (Å)	94	128	161	217
crater depth (Å)	25	33	49	62
sputtered mass (Da) [a]	1135	10910	24689	55628
sputtered + rim (Da) [b]	9674	26694	68699	219697
ratio [a]/[b]	0.12	0.41	0.36	0.25
sputtered molecules	0	3	7	19 (2 dimers)

^a In all cases, the values have been obtained for a single trajectory.

with increasing energy. The increase of the crater diameter is well fitted by a power function with an exponent of 1/3 and the depth, by a power function with a slightly larger exponent (0.4). These numbers mirror the observation that the crater is a

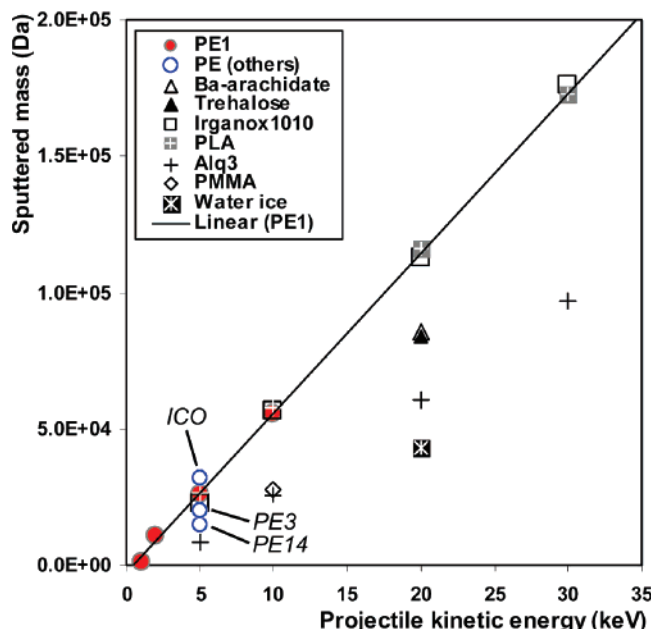


Figure 13. Sputtered mass (Da) per impact as a function of the projectile energy. The values calculated from MD simulations are signified by full red (PE1) and open blue circles (ICO, PE3, and PE14). The experimental values obtained from the literature correspond to Irganox 1010,³⁸ polylactic acid,³⁸ aluminum tris-(8-hydroxyquinoline),³⁸ polymethyl methacrylate,⁴² trehalose,³⁹ Ba-arachidate,⁴⁰ and water ice.⁴¹

slightly flattened hemisphere at low energy and it becomes a perfect hemisphere in the range 5–10 keV. When plotted as a function of projectile energy, the crater volume evolves almost linearly in the entire range of energies, with a slope value of $\sim 10^2 \text{ nm}^3/\text{keV}$.

The quantities of matter that are sputtered or redeposited in the rim exhibit a more complex variation (Table 4). Between the onset of sputtering (below 1 keV) and 2 keV, one observes a steep increase of the sputtered mass as a function of projectile energy. Beyond 2 keV, the sputtered mass increases more slowly and linearly (Figure 13), with an increment of $\sim 5.6 \text{ kDa}/\text{keV}$ (Figure 13). In the same energy range, the mass of matter that is above the surface plane after 20 ps, i.e., ejected or forming the crater rim, increases quasilinearly. As a result, the ratio of sputtered matter versus [sputtered + redeposited] matter increases steeply in the range 1–2 keV and decreases slowly afterward, as indicated in Table 4. In terms of displaced matter amounts, the energy of 2 keV, corresponding to the maximum of this ratio, can be considered as the energy for which the projectile is the most efficient at sputtering target material. Over the whole range of energies, the total sputtered mass remains inferior to the mass of material displaced to form the rim.

The linear increase of the sputtering yield (sputtered mass) with the projectile kinetic energy K above a certain threshold can be tentatively traced back to the origin of the cluster-surface interaction. Indeed, it was shown in a previous article that the volume of the energized region at 200 fs is roughly proportional to the projectile energy for the C_{60} bombardment of polystyrene oligomer (atomistic model) and icosane (coarse-grained model) solids.¹⁸ Within the formalism of the MEDF model,¹³ derived from fluid dynamics calculations, it means that the radius of the track, R_{cyl} , evolves as $\sim K^{1/3}$ (because the volume is almost spherical) and the average energy density is almost constant over the range of investigated energies (i.e., the average excitation energy with respect to the cohesive binding energy of the solid $\tilde{E} = E_{\text{exc}}/U_0$ is also constant). Because the yield in the MEDF model is directly proportional to $R_{\text{cyl}}^3 \tilde{E}$, and, in turn,

to K , this model seems appropriate to describe the linear evolution of our calculated yields beyond 2 keV. A more quantitative analysis of our previous and current results in the framework of the MEDF model is outside the scope of this article.

Recent experiments obtained with fullerene projectiles bombarding various organic targets also tend to show that the sputtered volume/mass increases linearly with the projectile energy, at least in the range 5–30 keV.³⁸ In Figure 13, values of sputtered mass per primary ion, available from the literature for a series of samples, are plotted with the results of our simulations. The sputtering yields of trehalose,³⁹ Ba-arachidate,⁴⁰ and water ice⁴¹ have been obtained from the Penn State group and those of Irganox 1010, polylactic acid (PLA, $M_w = 50\,000$) and aluminum tris-(8-hydroxyquinoline) (Alq3), from the National Physical Laboratory group.³⁸ The value reported for polymethyl methacrylate (PMMA; $M_w = 540\,000$) at 10 keV is from the measurements of Möllers et al. at 20 °C (the sputter yield of PMMA is T°-sensitive).⁴²

The linear regression drawn from the values calculated for PE1 (1388 Da) merges with the experimental values measured by Shard et al. for the polymer additive, Irganox 1010 (1177 Da) and for PLA.³⁸ The yields of trehalose and Ba-arachidate are slightly lower. The yields measured for Alq3, an organometallic compound, for water ice films and for PMMA are significantly lower. Unlike Irganox 1010 and PLA, Alq3 is found to accumulate damage and its sputtering yield changes from that of organic materials to that of inorganic materials (such as silicon) upon continuous bombardment. Even though their density is in the same range (water ice, ~ 0.92 ; Alq3, ~ 1.42), both Alq3 and water ice are quite different from the other considered organic and polymeric solids in terms of physical properties (cohesive energy, viscoelastic properties). The fact that the sputtering yield of these compounds is significantly off the curve confirms the effect of the sample nature on the ion-target interaction and secondary emission predicted by other theoretical studies.^{13,16} The case of PMMA is particularly interesting because it is the only high-molecular weight polymer in the considered set of samples, yet it is difficult to rationalize. On the one hand, the lower yield of PMMA in comparison with Irganox 1010 seems to confirm the trend from the simulations that higher molecular weights lead to lower yields. On the other hand, PMMA is well-known as a resist that unzips under irradiation, and the same study of Möllers et al. shows the strong dependence of its yield as a function of temperature.⁴² For example, the sputtering yield of PMMA at -140 °C is about half that measured at 20 °C. This sensitivity of PMMA, mirroring the complex chemical reactions that heat and/or various types of irradiation conditions (including lasers)⁴³ can induce in its structure, makes it a too complex material for our sputtering model at this stage. Overall, the comparison of Figure 13 indicates that the coarse-grained PE1 system constitutes an adequate generic model for molecular solids made of kilodalton molecules. It predicts both the linear evolution of the yield with projectile energy beyond a threshold value and, quantitatively, the total sputtered mass at a given energy. Beyond these predictions, our model systems explain some of the yield variation related to finer details of the sample structure (ICO, PE1, PE3, and PE14).

Combining our discussion about intact molecular emission with the calculated and measured projectile energy dependences of the yield and crater sizes, it becomes clear why molecules larger than 10–20 kDa are still very difficult to observe in SIMS of bulk organic samples, even with buckminsterfullerene

projectiles. In the considered energy range, the limited size of the annular volume from which heavy damage is excluded and the momentum gradient in the forming crater leading to high internal energies, associated to the larger binding energies and/or more pronounced entanglement of larger molecules constitute strong constraints that appear almost impossible to overcome. Indeed, to our knowledge, there is no SIMS report showing the detection of such large molecular ions from bulk organic samples.

4. Conclusion

Buckminsterfullerene projectiles with 1–10 keV of translational energy create hemispherical craters at the surface of polymeric materials and displace a volume of matter of about 50 nm³ per keV. In addition to effects already shown with other types of targets under C₆₀ bombardment, our results describe certain behaviors that are specific to the long linear molecules constituting the archetype of polymers. Upon 5 keV bombardment, a fraction of the displaced polymer chains, inversely proportional to the molecular size, is desorbed, whereas another fraction redeposits into a rim or remains dangling in the gas phase for more than 50 ps, especially for high MW molecules. In parallel, the sputtered volume and, to a smaller extent, the crater size decrease with the length of the polymer chains. The simulations help us to define three criteria for intact molecular ejection upon fullerene bombardment: The molecule should not intersect the high-energy core of the projectile track, it should be entirely confined in the volume that will be displaced (the crater) and it should initially sit in the zone where most of the target atoms receive upward momentum (top 30 Å upon 5 keV bombardment). The large-scale nature of the interaction, adequately described using a coarse-grained MD model, explains the large yields of sputtered molecular species usually measured upon keV fullerene bombardment of organic materials. The calculated masses of ejected material are in agreement with recent experimental measurements.

Acknowledgment. The authors thank Drs. I. Gilmore and A. Shard for communicating their detailed experimental results concerning Irganox 1010, polylactic acid, and aluminum tris-(8-hydroxyquinoline) shown in Figure 13. The financial support of the National Science Foundation through the Chemistry Division is gratefully acknowledged by B.J.G. A.D. also acknowledges the Belgian Fonds National pour la Recherche Scientifique and the European Network of Excellence NANO-BEAMS for financial and travel support. Additional computational resources were provided by the Academic Services and Emerging Technologies (ASET) of Penn State University. We are also indebted to the ASET staff for assistance with the Lion-xo and Lion-xl clusters. Prof. J. Kubicki is gratefully acknowledged for granting us access to the Accelrys Cerius² software package. The theoretical and computational biophysics group of the University of Illinois at Urbana-Champaign is acknowledged for the development and free access to the visualization software VMD.

References and Notes

- (1) Vickerman, J. C. In *ToF-SIMS: Surface Analysis by Mass Spectrometry*; Vickerman, J. C., Briggs, D., Eds.; SurfaceSpectra/IMPublications: Chichester, U.K. 2001; Chapter 1.
- (2) Gillen, G.; Roberson, S. *Rapid Commun. Mass Spectrom.* **1998**, 12, 1303.
- (3) Brunelle, A.; Della-Negra, S.; Depauw, J.; Jacquet, D.; Le Beyec, Y.; Pautrat, M.; Baudin, K.; Andersen, H. H. *Phys. Rev. A* **2001**, 63, 236, 1.
- (4) Kollmer, F. *Appl. Surf. Sci.* **2004**, 231–232, 153.
- (5) Weibel, D.; Wong, S.; Lockyer, N.; Blenkinsopp, P.; Hill, R.; Vickerman, J. C. *Anal. Chem.* **2003**, 75, 1754.
- (6) Winograd, N. *Anal. Chem.* **2005**, 77, 143A.
- (7) Van Stipdonk, M. In *ToF-SIMS: Surface Analysis by Mass Spectrometry*; Vickerman, J. C., Briggs, D., Eds.; SurfaceSpectra/IM Publications: Chichester, U.K., 2001; Chapter 12.
- (8) Postawa, Z.; Czerwinski, B.; Szewczyk, M.; Smiley, E. J.; Wino-grad, N.; Garrison, B. *J. Anal. Chem.* **2003**, 75, 4402.
- (9) Krantzman, K. D.; Kingsbury, D. B.; Garrison, B. *J. Nucl. Instrum. Methods B* **2007**, 255, 238.
- (10) Kerford, M.; Webb, R. P. *Nucl. Instrum. Meth. Phys. Res. B* **2001**, 180, 44.
- (11) Smiley, E.; Winograd, N.; Garrison, B. *J. Appl. Surf. Sci.* **2006**, 252, 6436.
- (12) Smiley, E.; Postawa, Z.; Wojciechowski, I. A.; Winograd, N.; Garrison, B. *J. Anal. Chem.* **2007**, 79, 494.
- (13) Russo, M. J., Jr.; Garrison, B. *J. Anal. Chem.* **2006**, 78, 7206.
- (14) Russo, M. J., Jr.; Szakal, C.; Kozole, J.; Winograd, N.; Garrison, B. *J. Anal. Chem.* **2007**, in press.
- (15) Jakas, M. M.; Bringa, E. M.; Johnson, R. E. *Phys. Rev. B* **2002**, 65, 165425.
- (16) Anders, C.; Kirihata, H.; Yamaguchi, Y.; Urbassek, H. M. *Nucl. Instrum. Meth. Phys. Res. B* **2007**, 255, 247.
- (17) Garrison, B. J. In *ToF-SIMS: Surface Analysis by mass spectrometry*; Vickerman, J. C., Briggs, D., Eds.; SurfaceSpectra/IMPublications: Chichester, U.K., 2001; p 223.
- (18) Delcorde, A.; Garrison, B. *J. Nucl. Instrum. Meth. Phys. Res. B* **2007**, 255, 223.
- (19) <http://physchem.ox.ac.uk/MSDS/EI/eicosane.html>.
- (20) http://www.chem007.com/specification_d/chemicals/supplier/cas-n-Eicosane.asp.
- (21) <http://www.sigmaldrich.com/>.
- (22) Garrison, B. J.; Kodali, P. B. S.; Srivastava, D. *Chem. Rev.* **1996**, 96, 1327.
- (23) Hautman, J.; Klein, M. L. *J. Chem. Phys.* **1989**, 91, 4994.
- (24) Balasubramanian, S.; Klein, M. L.; Siepmann, J. I. *J. Chem. Phys.* **1995**, 103, 3184.
- (25) Girifalco, L. A.; Weizer, V. G. *Phys. Rev.* **1959**, 114, 687.
- (26) Brenner, D. W.; Shenderova, O. A.; Harrison, J. A.; Stuart, S. J.; Ni, B.; Sinnott, S. B. *J. Phys.: Condens. Matter* **2002**, 14, 783.
- (27) Delcorde, A. In *ToF-SIMS: Surface Analysis by Mass Spectrometry*; Vickerman, J. C., Briggs, D., Eds.; SurfaceSpectra/IMPublications: Chichester, U.K., 2001; p 161.
- (28) Beardmore, K.; Smith, R. *Nucl. Instrum. Methods Phys. Res., Sect. B* **1995**, 102, 223.
- (29) Delcorde, A.; Garrison, B. *J. J. Phys. Chem. B* **2003**, 107, 2297.
- (30) Zhigilei, L. V.; Kodali, P. B.; Garrison, B. *J. J. Phys. Chem. B* **1998**, 102, 2845.
- (31) Urbassek, H. M.; Waldeer, K. Th. *Phys. Rev. Lett.* **1991**, 67, 105.
- (32) Wojciechowski, I. A.; Garrison, B. *J. J. Phys. Chem. A* **2006**, 110, 1389.
- (33) Delcorde, A.; Bertrand, P. *Nucl. Instrum. Meth. Phys. Res. B* **1996**, 115, 246.
- (34) Czerwinski, B.; Delcorde, A.; Garrison, B. J.; Samson, R.; Winograd, N.; Postawa, Z. *Appl. Surf. Sci.* **2006**, 252, 6419.
- (35) Delcorde, A.; Garrison, B. *J. J. Phys. Chem. B* **2004**, 108, 15652.
- (36) Postawa, Z.; Czerwinski, B.; Szewczyk, M.; Smiley, E. J.; Wino-grad, N.; Garrison, B. *J. J. Phys. Chem. B* **2004**, 108, 7831.
- (37) Delcorde, A.; Bertrand, P.; Garrison, B. *J. Nucl. Instrum. Meth. Phys. Res. B* **2000**, 171, 277.
- (38) Shard, A. G.; Brewer, P. J.; Green, F. M.; Gilmore, I. S. *Surf. Interface Anal.* **2007**, 39, 294.
- (39) Cheng, J.; Wucher, A.; Winograd, N. *J. Phys. B* **2006**, 110, 8329.
- (40) Sostarecz, A. G.; Sun, S.; Szakal, C.; Wucher, A.; Winograd, N. *Appl. Surf. Sci.* **2004**, 231, 179.
- (41) Wucher, A.; Sun, S.; Szakal, C.; Winograd, N. *Anal. Chem.* **2004**, 76, 7234.
- (42) Möllers, R.; Tuccitto, N.; Torrisi, V.; Niehuis, E.; Licciardello, A. *Appl. Surf. Sci.* **2006**, 252, 6509.
- (43) Prasad, M.; Conforti, P. F.; Garrison, B. J.; Yingling, Y. G. *Appl. Surf. Sci.* **2007**, 253, 6382.